THE JOURNAL OF PHYSICAL CHEMISTRY C

Article

pubs.acs.org/JPCC

Driven Liouville von Neumann Approach for Time-Dependent Electronic Transport Calculations in a Nonorthogonal Basis-Set Representation

Tamar Zelovich,[†,§] Leeor Kronik,[‡] and Oded Hod*[,†]

[†]Department of Physical Chemistry, School of Chemistry, The Raymond and Beverly Sackler Faculty of Exact Sciences and The Sackler Center for Computational Molecular and Materials Science, Tel Aviv University, Tel Aviv 6997801, Israel

[‡]Department of Materials and Interfaces, Weizmann Institute of Science, Rehovoth 76100, Israel

Supporting Information

ABSTRACT: A nonorthogonal localized basis-set implementation of the driven Liouville von Neumann (DLvN) approach is presented. The method is based on block-orthogonalization of the Hamiltonian and overlap matrix representations, yielding non-overlapping blocks that correspond to the various system sections. An extended Hückel description of gold/benzene-dithiol/gold and gold/pyridine-dithiol/gold junctions is used to demonstrate the performance of the method. The presented generalization is an important milestone toward using the DLvN approach for performing accurate dynamic electronic transport calculations in realistic model systems, based on density functional theory packages that rely on atom-centered basis-set representations.

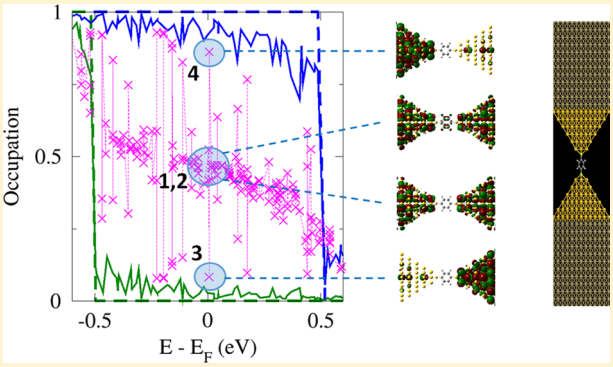

INTRODUCTION

The study of electronic transport through molecular-scale junctions is at the heart of the field of molecular electronics.[1−4] Over the past four decades this field has matured to a point where measurements and calculations of steady-state transport characteristics of individual molecules are routinely performed in many laboratories.[5−7] Different aspects, such as conductance switching,[8−12] rectification,[13−18] thermo-power effects,[19−24] interference effects,[25−28] chemical composition,[29] and lead−molecule coupling schemes,[18,30−33] have been explored aiming to realize a molecular device exhibiting the desired functionality and efficiency.

Experimental efforts to study molecular junctions subject to time-dependent perturbations are currently at their infancy. This is probably a result of the technical complexity involved in such measurements. Here, theory and computation may offer valuable support both in guiding experiments toward promising molecular setups and optimal operation conditions and in the interpretation and understanding of experimental results. To this end a variety of methods, too vast to review here in detail, have been developed for modeling electron dynamics in single molecule junctions. Many of these methods rely on model Hamiltonians that provide valuable information regarding general transport phenomena but cannot describe the dynamical behavior of specific junctions; see, e.g., refs 34−43. Other approaches explicitly consider the chemical composition and structure of the studied system, thus allowing for direct comparison with realistic experimental scenarios; see, e.g., refs 44−56.

Recently, we have suggested that these two views can be combined. To this end, the driven Liouville von Neumann (DLvN) approach[57,58] for calculating time-dependent[59] electronic transport through atomistic junction models has been developed. Within this approach, nonequilibrium boundary conditions, mimicking the effects of coupling to external particle and heat reservoirs, are imposed at the edges of finite junction models, thus effectively "opening" the system. To avoid computational complexity during the proof-of-concept stages of the development of the DLvN approach, simple Hamiltonian models, avoiding explicit use of a basis-set, have been employed.[57,58] However, simulations of electron dynamics in realistic molecular junctions often involve a nonorthogonal atom-centered basis-set representation of the corresponding time-dependent electronic wave functions.[60−65] Such a representation presents a difficulty for the DLvN method as lead and molecule eigenstates are not orthogonal, an issue elaborated below.

In the present paper, we extend the applicability of the DLvN approach to nonorthogonal basis-set representations. To overcome the inter-subblock basis-function mixing problem we adopt the recently proposed block-orthogonalization procedure of Kwok et al.[62] We validate the methodology by studying the simple case of transport through a hydrogen chain, described by an extended Hückel (EH) Hamiltonian

Received: April 15, 2016
Revised: June 9, 2016
Published: June 20, 2016

DOI: 10.1021/acs.jpcc.6b03838
J. Phys. Chem. C 2016, 120, 15052−15062

model. The latter is then used to study the dynamic transport characteristics of benzene- and pyridine-dithiol molecules bridging two gold electrodes. This demonstrates the applicability of the method to simulations of electron dynamics in realistic molecular junction models within a nonorthogonal basis-set representation.

METHOD

The driven Liouville von Neumann approach uses a finite system, consisting of a molecule and lead models, to study electronic transport through molecular junctions. For a two-lead setup, the system is artificially divided into three sections including the left (L) and right (R) leads and the extended molecule (EM). The latter is the molecule augmented by lead subsections chosen to be sufficiently large such that the electronic properties of the resulting extended molecule are converged with respect to their size, to within a required accuracy. The lead subsections further act as buffer regions that minimize the interaction of the molecular region with the lead models, where driving terms are applied as described below. With this partition, if one chooses an atom-centered basis-set representation, the real-space overlap and Hamiltonian matrix representations take the following block form

$$\mathbf{S} = \begin{pmatrix} \mathbf{S}_{\mathrm{L}} & \mathbf{S}_{\mathrm{L,EM}} & \mathbf{0} \\ \mathbf{S}_{\mathrm{EM,L}} & \mathbf{S}_{\mathrm{EM}} & \mathbf{S}_{\mathrm{EM,R}} \\ \mathbf{0} & \mathbf{S}_{\mathrm{R,EM}} & \mathbf{S}_{\mathrm{R}} \end{pmatrix}; \mathbf{H} = \begin{pmatrix} \mathbf{H}_{\mathrm{L}} & \mathbf{V}_{\mathrm{L,EM}} & \mathbf{0} \\ \mathbf{V}_{\mathrm{EM,L}} & \mathbf{H}_{\mathrm{EM}} & \mathbf{V}_{\mathrm{EM,R}} \\ \mathbf{0} & \mathbf{V}_{\mathrm{R,EM}} & \mathbf{H}_{\mathrm{R}} \end{pmatrix} \tag{1}$$

where $\mathbf{S}_{\mathrm{L}}$, $\mathbf{S}_{\mathrm{R}}$, $\mathbf{S}_{\mathrm{EM}}$ and $\mathbf{H}_{\mathrm{L}}$, $\mathbf{H}_{\mathrm{R}}$, $\mathbf{H}_{\mathrm{EM}}$ are the real-space overlap and Hamiltonian matrix blocks of the left and right lead sections and the extended molecule, respectively. $\mathbf{S}_{\mathrm{L,EM}} = \mathbf{S}_{\mathrm{EM,L}}^{\dagger}$, $\mathbf{S}_{\mathrm{R,EM}} = \mathbf{S}_{\mathrm{EM,R}}^{\dagger}$, $\mathbf{V}_{\mathrm{L,EM}} = \mathbf{V}_{\mathrm{EM,L}}^{\dagger}$, and $\mathbf{V}_{\mathrm{R,EM}} = \mathbf{V}_{\mathrm{EM,R}}^{\dagger}$ are the corresponding overlap and coupling matrices between the extended molecule section and the left and right leads, and we neglect any direct interlead orbital overlap ($\mathbf{S}_{\mathrm{L,R}} = \mathbf{S}_{\mathrm{R,L}}^{\mathrm{T}} = 0$) and Hamiltonian coupling ($\mathbf{V}_{\mathrm{L,R}} = \mathbf{V}_{\mathrm{R,L}}^{\dagger} = 0$). The latter assumption is valid for spatially well-separated leads.

The real-space Hamiltonian matrix of the whole system is first transformed to the basis of eigenfunctions of the individual system sections. In this representation, non-equilibrium single-particle lead state occupations, obeying Fermi–Dirac statistics with the chemical potential and electronic temperature of the respective reservoirs, can be readily enforced.[57] Using a nonorthogonal basis-set, however, the molecular orbitals (MOs) of the individual system sections (L, EM, and R) are not mutually orthogonal when the subsections are brought into contact. This intrinsic mixing between the lead and extended molecule MOs implies that the boundary conditions applied to the lead states explicitly involve the extended molecule MOs as well. In turn, this introduces unphysical effects within the scattering region of interest, thereby hindering the validity of the predictions.

To solve this problem, we adopt the block orthogonalziation method of Kwok et al.,[62] which uses a transformation of the form

$$\mathbf{U}_{\mathrm{b}} = \begin{pmatrix} \mathbf{I}_{\mathrm{L}} & -\mathbf{S}_{\mathrm{L}}^{-1}\mathbf{S}_{\mathrm{L,EM}} & \mathbf{0} \\ \mathbf{0} & \mathbf{I}_{\mathrm{EM}} & \mathbf{0} \\ \mathbf{0} & -\mathbf{S}_{\mathrm{R}}^{-1}\mathbf{S}_{\mathrm{R,EM}} & \mathbf{I}_{\mathrm{R}} \end{pmatrix} \tag{2}$$

with $\mathbf{I}_{i=\mathrm{L,EM,R}}$ being a unit matrix of dimensions $i \times i$, to transform the atom-centered orbital basis of the extended molecule section, making it mutually orthogonal to the left and right lead basis functions. Under this transformation, the real-space overlap matrix of the whole system obtains the following block diagonal form[62]

$$\begin{aligned} \tilde{\mathbf{S}} = \mathbf{U}_{\mathrm{b}}^{\dagger}\mathbf{S}\mathbf{U}_{\mathrm{b}} &= \begin{pmatrix} \mathbf{S}_{\mathrm{L}} & \mathbf{0} & \mathbf{0} \\ \mathbf{0} & \mathbf{S}_{\mathrm{EM}} - \mathbf{S}_{\mathrm{EM,L}}\mathbf{S}_{\mathrm{L}}^{-1}\mathbf{S}_{\mathrm{L,EM}} - \mathbf{S}_{\mathrm{EM,R}}\mathbf{S}_{\mathrm{R}}^{-1}\mathbf{S}_{\mathrm{R,EM}} & \mathbf{0} \\ \mathbf{0} & \mathbf{0} & \mathbf{S}_{\mathrm{R}} \end{pmatrix} \\ &\equiv \begin{pmatrix} \mathbf{S}_{\mathrm{L}} & \mathbf{0} & \mathbf{0} \\ \mathbf{0} & \tilde{\mathbf{S}}_{\mathrm{EM}} & \mathbf{0} \\ \mathbf{0} & \mathbf{0} & \mathbf{S}_{\mathrm{R}} \end{pmatrix} \end{aligned} \tag{3}$$

and the Hamiltonian matrix reads

$$\tilde{\mathbf{H}} = \mathbf{U}_{\mathrm{b}}^{\dagger}\mathbf{H}\mathbf{U}_{\mathrm{b}} = \begin{pmatrix} \mathbf{H}_{\mathrm{L}} & \mathbf{V}_{\mathrm{L,EM}} - \mathbf{H}_{\mathrm{L}}\mathbf{S}_{\mathrm{L}}^{-1}\mathbf{S}_{\mathrm{L,EM}} & \mathbf{0} \\ \mathbf{V}_{\mathrm{EM,L}} - \mathbf{S}_{\mathrm{EM,L}}\mathbf{S}_{\mathrm{L}}^{-1}\mathbf{H}_{\mathrm{L}} & \tilde{\mathbf{H}}_{\mathrm{EM}} & \mathbf{V}_{\mathrm{EM,R}} - \mathbf{S}_{\mathrm{EM,R}}\mathbf{S}_{\mathrm{R}}^{-1}\mathbf{H}_{\mathrm{R}} \\ \mathbf{0} & \mathbf{V}_{\mathrm{R,EM}} - \mathbf{H}_{\mathrm{R}}\mathbf{S}_{\mathrm{R}}^{-1}\mathbf{S}_{\mathrm{R,EM}} & \mathbf{H}_{\mathrm{R}} \end{pmatrix} = \begin{pmatrix} \mathbf{H}_{\mathrm{L}} & \tilde{\mathbf{V}}_{\mathrm{L,EM}} & 0 \\ \tilde{\mathbf{V}}_{\mathrm{EM,L}} & \tilde{\mathbf{H}}_{\mathrm{EM}} & \tilde{\mathbf{V}}_{\mathrm{EM,R}} \\ \mathbf{0} & \tilde{\mathbf{V}}_{\mathrm{R,EM}} & \mathbf{H}_{\mathrm{R}} \end{pmatrix} \tag{4}$$

where

$$\begin{aligned} \tilde{\mathbf{H}}_{\mathrm{EM}} \equiv \mathbf{H}_{\mathrm{EM}} &- \mathbf{S}_{\mathrm{EM,L}}\mathbf{S}_{\mathrm{L}}^{-1}\mathbf{V}_{\mathrm{L,EM}} - \mathbf{V}_{\mathrm{EM,L}}\mathbf{S}_{\mathrm{L}}^{-1}\mathbf{S}_{\mathrm{L,EM}} \\ &- \mathbf{V}_{\mathrm{EM,R}}\mathbf{S}_{\mathrm{R}}^{-1}\mathbf{S}_{\mathrm{R,EM}} - \mathbf{S}_{\mathrm{EM,R}}\mathbf{S}_{\mathrm{R}}^{-1}\mathbf{V}_{\mathrm{R,EM}} \\ &+ \mathbf{S}_{\mathrm{EM,L}}\mathbf{S}_{\mathrm{L}}^{-1}\mathbf{H}_{\mathrm{L}}\mathbf{S}_{\mathrm{L}}^{-1}\mathbf{S}_{\mathrm{L,EM}} + \mathbf{S}_{\mathrm{EM,R}}\mathbf{S}_{\mathrm{R}}^{-1}\mathbf{H}_{\mathrm{R}}\mathbf{S}_{\mathrm{R}}^{-1}\mathbf{S}_{\mathrm{R,EM}} \end{aligned} \tag{5}$$

Notably, the overlap and Hamiltonian diagonal blocks corresponding to the left and right leads are unaffected by this transformation ($\tilde{\mathbf{S}}_{\mathrm{L}} = \mathbf{S}_{\mathrm{L}}$, $\tilde{\mathbf{S}}_{\mathrm{R}} = \mathbf{S}_{\mathrm{R}}$, $\tilde{\mathbf{H}}_{\mathrm{L}} = \mathbf{H}_{\mathrm{L}}$, $\tilde{\mathbf{H}}_{\mathrm{R}} = \mathbf{H}_{\mathrm{R}}$). This allows us to enforce the single-particle lead state occupation boundary conditions as in the orthogonal basis-set representation case while avoiding the complexity of inter-section MO mixing. To this end, we apply the unitary site-to-state transformation of the form

$$\mathbf{U} = \begin{pmatrix} \mathbf{U}_{\mathrm{L}} & \mathbf{0} & \mathbf{0} \\ \mathbf{0} & \mathbf{U}_{\mathrm{EM}} & \mathbf{0} \\ \mathbf{0} & \mathbf{0} & \mathbf{U}_{\mathrm{R}} \end{pmatrix} \tag{6}$$

to $\tilde{\mathbf{S}}$ and $\tilde{\mathbf{H}}$. Here, $\mathbf{U}_{i=\mathrm{L,EM,R}}$ are unitary matrices constructed from the eigenvectors of the generalized eigenvalue equations, $\tilde{\mathbf{H}}_i c = \epsilon \tilde{\mathbf{S}}_i c$, such that $\tilde{\tilde{\mathbf{H}}}_i = \mathbf{U}_i^{\dagger}\tilde{\mathbf{H}}_i\mathbf{U}_i$ are diagonal matrices holding the eigenstates of the isolated ith section on their diagonal and $\mathbf{U}_i^{\dagger}\tilde{\mathbf{S}}_i\mathbf{U}_i = \mathbf{I}_i$. This constitutes a transformation to the basis of single-particle eigenstates of the individual system sections (L, EM, and R).

DOI: 10.1021/acs.jpcc.6b03838
J. Phys. Chem. C 2016, 120, 15052−15062

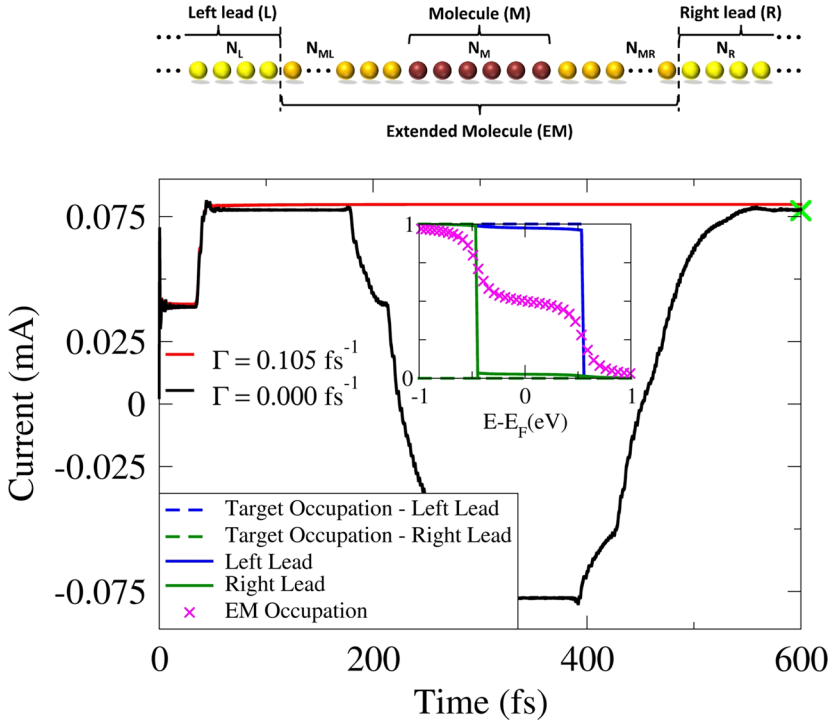

Figure 1. Time-dependent transport through a uniform hydrogen chain model. Upper panel: Schematic representation of the hydrogen chain junction model. The left and right leads are represented by finite elongated hydrogen chains (yellow spheres). The molecule (maroon spheres) is augmented by lead sections (orange spheres) to form the extended molecule. N_L, N_M, and N_R are the number of hydrogen atoms used to represent the left lead, molecule, and right lead models, respectively. N_{ML} and N_{MR} are the number of extended molecule atoms on the left and right of the molecule, respectively. Lower panel: Time-dependent current through a system of dimensions $N_L = N_R = 300$, $N_{ML} = N_{MR} = 50$, $N_M = 20$, and a uniform interatomic distance of $d_{CC} = 2$ Å, calculated at a bias voltage of $V_b = 1.0$ V and lead electronic temperatures of $T_L = T_R = 0$ K, using an adaptive time step fifth-order Runge−Kutta propagation scheme for eq 8. The initial conditions impose Fermi−Dirac state occupations on the left and right lead models with chemical potentials and electronic temperatures of the corresponding implicit external reservoir. Specifically, the leftmost N_L atoms experience a chemical potential of $\mu_L = E_F + 0.5V_b$, and the rightmost N_R atoms experience a chemical potential of $\mu_R = E_F - 0.5V_b$, where the Fermi energy, E_F, is chosen as the average of the highest occupied and lowest unoccupied molecular orbital energies of the entire finite junction model. In the extended molecule, an initial Fermi−Dirac distribution with chemical potential $\mu_M = E_F$ and electronic temperature of $T_M = 0$ K is used. The black and red lines represent results of microcanonical ($\Gamma = 0$) and DLvN ($\Gamma = 0.105$ fs^{-1}) calculations, respectively. The green X mark represents the steady-state current obtained via the Landauer approach (see Appendix B).[85,86] Inset: Left lead (full blue line), right lead (full green line), and extended molecule (purple x symbols) steady-state occupations. The target single-particle lead state occupations (diagonal elements of $\tilde{\tilde{\boldsymbol{\rho}}}^0_{L/R}$) are represented by the blue (left lead) and green (right lead) dashed-line step functions.

In the single-particle state representation, the overlap matrix becomes the identity matrix $\tilde{\tilde{\mathbf{S}}} = \mathbf{U}^\dagger\tilde{\mathbf{S}}\mathbf{U} = \mathbf{I}$, and the Hamiltonian matrix is written as

$$\tilde{\tilde{\mathbf{H}}} = \mathbf{U}^\dagger\tilde{\mathbf{H}}\mathbf{U} = \begin{pmatrix} \mathbf{U}_L^\dagger\mathbf{H}_L\mathbf{U}_L & \mathbf{U}_L^\dagger\tilde{\mathbf{V}}_{L,EM}\mathbf{U}_{EM} & \mathbf{0} \\ \mathbf{U}_{EM}^\dagger\tilde{\mathbf{V}}_{EM,L}\mathbf{U}_L & \mathbf{U}_{EM}^\dagger\tilde{\mathbf{H}}_{EM}\mathbf{U}_{EM} & \mathbf{U}_{EM}^\dagger\tilde{\mathbf{V}}_{EM,R}\mathbf{U}_R \\ \mathbf{0} & \mathbf{U}_R^\dagger\tilde{\mathbf{V}}_{R,EM}\mathbf{U}_{EM} & \mathbf{U}_R^\dagger\mathbf{H}_R\mathbf{U}_R \end{pmatrix} \quad (7)$$

Here, the diagonal blocks represent the single-particle eigenstate energy manifolds of the various system sections, and the off-diagonal blocks represent the intermanifold coupling scheme.[58] Importantly, since $\tilde{\tilde{\mathbf{S}}}$ becomes the unit matrix and the direct interlead couplings in $\tilde{\tilde{\mathbf{H}}}$ remain eliminated, we may apply the DLvN equation of motion (EOM),[57] originally developed for tight-binding model Hamiltonians, to calculate the dynamic electronic transport through the system under open boundary conditions within the nonorthogonal basis-set representation. Specifically,

$$\frac{d}{dt}\tilde{\tilde{\boldsymbol{\rho}}}(t) = -\frac{i}{\hbar}[\tilde{\tilde{\mathbf{H}}}, \tilde{\tilde{\boldsymbol{\rho}}}] - \Gamma\begin{pmatrix} \tilde{\tilde{\boldsymbol{\rho}}}_L(t) - \tilde{\tilde{\boldsymbol{\rho}}}_L^0 & \frac{1}{2}\tilde{\tilde{\boldsymbol{\rho}}}_{L,EM}(t) & \tilde{\tilde{\boldsymbol{\rho}}}_{L,R}(t) \\ \frac{1}{2}\tilde{\tilde{\boldsymbol{\rho}}}_{EM,L}(t) & 0 & \frac{1}{2}\tilde{\tilde{\boldsymbol{\rho}}}_{EM,R}(t) \\ \tilde{\tilde{\boldsymbol{\rho}}}_{R,L}(t) & \frac{1}{2}\tilde{\tilde{\boldsymbol{\rho}}}_{R,EM}(t) & \tilde{\tilde{\boldsymbol{\rho}}}_R(t) - \tilde{\tilde{\boldsymbol{\rho}}}_R^0 \end{pmatrix} \quad (8)$$

Here, $\tilde{\tilde{\boldsymbol{\rho}}}$ is the single-particle reduced density matrix in the state representation; $\tilde{\tilde{\boldsymbol{\rho}}}^0_{L/R}$ are diagonal density matrix blocks "encoding" the equilibrium Fermi−Dirac state occupation distribution of the left and right leads, respectively, with the appropriate chemical potential and electronic temperature; and Γ is the driving rate. Full details and derivations of this equation can be found in refs 57−59 and 66. Briefly, the DLvN EOM augments the unitary dynamics (represented by the commutator on the right-hand side of eq 8) with a term that drives the density at the system boundaries toward a

DOI: 10.1021/acs.jpcc.6b03838
J. Phys. Chem. C 2016, 120, 15052−15062

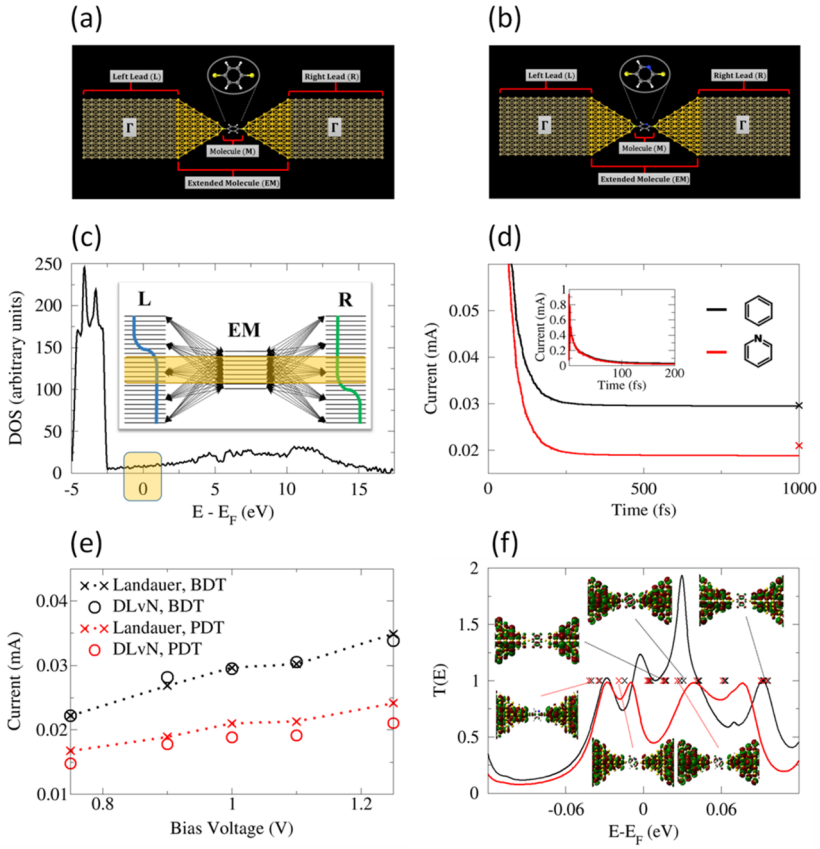

Figure 2. Time-dependent electronic transport in gold/benzene-dithiol/gold (a) and gold/pyridine-dithiol/gold (b) molecular junctions. The junctions consist of 596 gold-atom lead models (brown spheres) and 83 gold-atom lead sections (yellow spheres) within the extended molecule region on each side of the benzene/pyridine dithiol molecules (atomic coordinates are provided in the Supporting Information). The finite lead density of states, broadened by a Gaussian of width $\sigma = \hbar\Gamma = 0.052$ eV, is presented in panel (c), where the yellow rectangles represent the Fermi transport energy window (see inset for a state representation illustration of this energy window). Here, the origin of the energy axis is set to the center of the HOMO−LUMO energy gap of the isolated lead. The time-dependent currents calculated for the benzene (black) and pyridine (red) dithiol junctions, at a bias voltage of $V_b = 1.0$ V and electronic lead temperatures of $T_L = T_R = 0$ K, are depicted in panel (d). The initial conditions are similar to those described in the caption of Figure 1. The corresponding Landauer steady-state currents (see Appendix B) are designated by X marks with matching colors. Current vs bias voltage curves calculated from the DLvN steady-state currents obtained at a simulation time of 1 ps (circles) and the Landauer formalism (X marks) for the benzene (black) and pyridine (red) dithiol junctions are presented in panel (e), where dashed lines are added to guide the eye. Panel (f) presents the underlying transmittance probabilities of the two junctions in the vicinity of the Fermi energy, along with representative extended molecule MOs (using an isosurface value of 0.0075 atomic units) that bridge the two leads and can support current. X marks represent the eigenenergies of the extended molecule MOs in this range. Here, the origin of the energy axis is set to the center of the HOMO−LUMO energy gap of the entire (finite) system. The transmittance probability within the full Fermi transport window at $V_b = 1.0$ V and more MO illustrations are presented in the Supporting Information.

target density that represents the electron distribution of the corresponding reservoir. This enforces a stable charge imbalance at the boundaries, effectively "opening" the system and driving it toward a dynamic nonequilibrium current carrying state.

TESTING AND BENCHMARK EVALUATIONS

To demonstrate the performance of the DLvN dynamics within a nonorthogonal basis-set representation we use the semiempirical extended Hückel model,[67−71] which has been previously used to study transport calculations in molecular junctions.[72] Here, one defines an atom-centered Slater-type orbital (STO) basis-set[73,74] for the valence shell of each atom. The diagonal elements of the real-space Hamiltonian matrix are extracted from the atomic ionization potentials of the valence electrons; namely, the diagonal element corresponding to a given valence atomic orbital, i, is taken as the ionization potential of this atomic orbital, $H_{ii} = IP_i$. The off-diagonal Hamiltonian matrix elements are evaluated from their diagonal counterpart as $H_{ij} = 0.5(H_{ii} + H_{jj})KS_{ij}$. Here, $K = 1.75$ is the Wolfsberg−Helmholtz constant,[75] chosen to best fit the experimental data, and S_{ij} is the real-space overlap matrix between the various STOs. The overlap matrix elements are calculated analytically using a method developed by Guseinov et al.[76−81] For the overlap and Hamiltonian matrix element calculations, we adopt the STO and atomic ionization potential parameters of Hoffman.[67,69,82]

We consider first the simple case of transport through a uniform hydrogen atomic chain. The leads are represented by two 350 hydrogen atom chains bridged by a 20 atom chain section with a constant interatomic distance of $d_{CC} = 2$ Å throughout the system.[83] Within the extended Hückel minimal basis-set model, each hydrogen atom is assigned a single 1s-type STO resulting in overlap and Hamiltonian matrix representations of dimensions 720 × 720. We

DOI: 10.1021/acs.jpcc.6b03838
J. Phys. Chem. C 2016, 120, 15052−15062

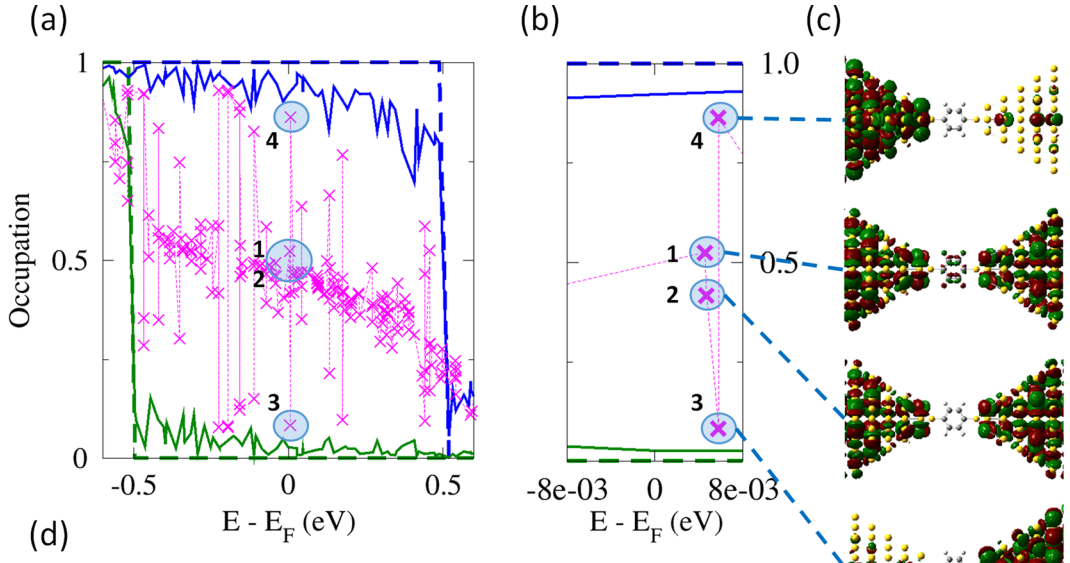

(d)

Number of State	Steady State Occupations	Effective Coupling to the Left Lead (eV)	Effective Coupling to the Right Lead (eV)
1	0.500	0.0038	0.0029
2	0.420	0.0034	0.0042
3	0.083	0.0007	0.0118
4	0.860	0.0117	0.0007

Figure 3. Steady-state single-particle state occupations of the various benzene−dithiol junction sections. (a) Left lead (solid blue line), right lead (solid green line), and extended-molecule (magenta x marks) steady-state occupations compared to the corresponding target lead-equilibrium step-function distributions (blue and green dashed lines, respectively). (b) Zoom in on the occupations of four specific consecutive extended-molecule states, denoted in (a). An illustration of the corresponding molecular orbitals within the extended molecule region is shown in (c), and their effective couplings to the left and right leads are given in (d).

propagate the DLvN equation of motion (eq 8) using the fifth-order Runge−Kutta scheme, with an adjustable time step.[84] The current through the bridge is calculated using the following expression (see Appendix A)

$$J = \frac{|e|}{\hbar}\sum_{n}^{N_{EM}}\{\sum_{m}^{N_R}\tilde{\tilde{\mathbf{V}}}_{EM,R}(n,m)Im[\tilde{\tilde{\boldsymbol{\rho}}}_{EM,R}(n,m)] - \sum_{m}^{N_L}\tilde{\tilde{\mathbf{V}}}_{EM,L}(n,m)Im[\tilde{\tilde{\boldsymbol{\rho}}}_{EM,L}(n,m)]\} \quad (9)$$

Here, e is the electron charge; $\hbar$ is the reduced Planck's constant; $\tilde{\tilde{\mathbf{V}}}_{EM,R/L}$ are the off-diagonal Hamiltonian matrix blocks coupling the extended molecule single-particle state manifold with the corresponding right and left lead states, respectively; and $\tilde{\tilde{\boldsymbol{\rho}}}_{EM,R/L}$ are the off-diagonal density matrix blocks representing the corresponding extended-molecule/lead state coherences.

The time-dependent current through a hydrogen chain model system, for a bias voltage of V_b = 1.0 V and lead electronic temperatures of $T_L = T_L$ = 0 K, is presented in Figure 1. The full black line represents a "microcanonical"[46] simulation, where no driving is applied (Γ = 0 fs^{-1}). As expected, after some transient dynamics (∼ 50 fs), dictated by the initial conditions, a quasi-steady-state (QSS) develops that matches the Landauer steady-state value (marked by the green x mark). This QSS remains stable until the wave packet is reflected from the edges of the finite model system back into the extended molecule region and current reversal occurs (at ∼225 fs). When turning on the driving term (Γ = 0.105 fs^{-1}) the system follows similar initial dynamics but develops a true steady state that matches the Landauer value. The inset of Figure 1 presents the eigenstate-resolved steady-state occupations in the left and right leads and the extended molecule. As can be seen, the lead state occupations are very close to their target step-function Fermi−Dirac populations with the corresponding chemical potentials.[87] The extended molecule populations form a smooth average between the lead state occupations within the Fermi transport window. This behavior resembles the tight-binding chain model results,[57] thus indicating the validity of the developed methodology.

Next, we turn to demonstrate the performance of the method for more realistic model junctions consisting of benzene dithiol (BDT, Figure 2a) and pyridine dithiol (PDT, Figure 2b) molecules bridging two gold leads.[88,89] The leads are represented by finite gold rods that form a tip-like structure near the molecular region. The formal division of the system into the left and right lead regions and the extended molecule, consisting of the benzene/pyridine dithiol molecules and their adjacent tip sections, is depicted in panels 2a and 2b. With the EH parameters used here, the electronic bandwidth of the finite lead models spans a range of 25 eV (see Figure 2c). The Fermi transport window (defined by the bias voltage, the equilibrium chemical potentials of the leads, and the lead electronic temperatures) is typically considerably narrower than this range (see yellow rectangles in Figure 2c). Therefore, we propagate only a

DOI: 10.1021/acs.jpcc.6b03838
J. Phys. Chem. C 2016, 120, 15052−15062

subset of single-particle states within the transport window and in its immediate vicinity and freeze the dynamics of the rest of the states. When converging the results with respect to the size of this dynamic range enclosing the transport window, this procedure considerably accelerates the computation at no loss of accuracy. Importantly, within the chosen dynamical energy range, a relatively uniform lead density of states is obtained (Figure 2c), thus justifying the choice of a single driving rate, Γ, to broaden the discrete set of finite lead model states into a continuum electronic structure. Specifically, for the junctions studied herein, we find that a value of $\Gamma = 0.08$ fs^{-1} reproduces well the Landauer steady-state current.

Figure 2d presents the time-dependent current through the benzene (black) and pyridine (red) junctions under a bias of 1.0 V and a gate voltage of −0.2 V simulated by a rigid shift of the onsite energies of the molecule atoms. The latter is applied in order to position the molecular eigenstates in a region of increased lead density of states within the model parameters. For both systems, after an initial current rise (see inset of Figure 2d), the system develops a stable steady state whose value matches well the Landauer result. The remaining deviations can be remedied by increasing the lead model size allowing for their state occupations to further approach the corresponding target equilibrium values. The benzene dithiol junction steady-state current is ∼50% higher than the corresponding pyridine dithiol value. These findings hold in a wide range of bias voltages, as can be seen in Figure 2e, where the current−voltage curves obtained for the two systems using the DLvN approach and the Landauer approach are compared. This can be explained by analyzing the electron transmittance probability through the junction (Figure 2f), calculated via nonequilibrium Green's function formalism (see Appendix B). Clearly, the pyridine junction exhibits a lower transmittance probability throughout the transport energy window. This is most pronounced near the Fermi energy, where the pyridine junction exhibits a transmittance probability close to 1 and the benzene junction shows a 2-fold larger transmittance probability, indicating the presence of two almost fully conducting channels. This can be attributed to the double degeneracy of the clockwise and anticlockwise particle-in-a-ring like benzene eigenstates, which is lifted in the case of pyridine. To demonstrate this, we plot in Figure 2f several MOs of the extended molecule that bridge the left and right leads and can carry current within the corresponding energy range. Specifically, near the BDT junction transmittance peak, located 0.03 eV above the Fermi energy, we find two MOs that span the whole extended molecule region with considerable weight residing on the BDT molecule itself. These facilitate the two open conduction channels that give rise to a transmittance probability of 2. When plotting the charge density variations for the two systems we also find negative charging of the BDT but no significant charging of PDT under bias voltage (see Supporting Information for further details).

Figure 3 depicts the steady-state single-particle state occupations of the various sections of the benzene dithiol junction. The left (full blue line) and right (full green line) lead model states follow the general envelope of the target step-function occupations (blue and green dashed lines, respectively) with the corresponding chemical potentials. The observed small undulations of the occupation function result from the variation of the different lead model states coupling to the extended molecule states. These can be further reduced by increasing the lead model size.[90] The extended molecule steady-state occupations (magenta x marks) follow a general pattern similar to that observed for the hydrogen chain junction (see inset of Figure 1) but exhibit strong fluctuations within the Fermi transport window. These can be attributed to asymmetric coupling of these states to the left and right lead state manifolds. To demonstrate this, we focus on four consecutive extended molecule states that exhibit large steady-state occupation variations (Figure 3b) and calculate their effective coupling to the left and right leads. To that end, we use a Fermi's golden rule based definition of the effective coupling: $Z_{L/R}(\varepsilon_n) = 2\pi\sum_q |\tilde{V}_{nq}^{L/R}|^2\ \delta(\varepsilon_n - \varepsilon_q^{L/R})$, where $\tilde{V}_{nq}^{L/R}$ are the coupling matrix elements between a bridge state of energy ε_n and a state of energy $\varepsilon_q^{L/R}$ of the left or right lead, as obtained by the "site-to-state" transformation, with the sum extending over all states in the relevant dynamic range of the lead.[58,59] The results are summarized in the table appearing in Figure 3d. Interestingly, the states marked by "1" and "2" are almost evenly coupled to both leads and hence have steady-state occupations close to 0.5. State "3" is 17 times more strongly coupled to the right lead (with the lower chemical potential) than to the left lead, resulting in a very low steady-state occupation of ∼0.083. On the contrary, the following state ("4") is 17 times more strongly coupled to the left lead (with higher chemical potential) than to the right lead resulting in a high steady-state occupation of ∼0.86. A similar behavior is found for all other MOs within the Fermi transport windows (see Supporting Information). This can also be qualitatively demonstrated by viewing the corresponding MOs (Figure 3c), where orbitals "1" and "2" span the entire extended molecule region, whereas orbitals "3" and "4" are localized on the right and left extended molecule sections, respectively. Notably, all single-particle state occupations are in the range of [0,1] indicating the conservation of N-representability and density matrix positivity throughout the simulation.[57,59,66]

CONCLUSIONS

In summary, we presented a nonorthogonal basis-set generalization of the driven Liouville von Neumann approach. The method addresses the problem of inter-subsystem orbital overlap by adopting a block diagonalization procedure that does not affect the lead basis. The performance of the method was demonstrated using time-dependent transport calculations for a hydrogen chain junction and for benzene and pyridine dithiol molecules bridging two gold leads, whose underlying electronic properties were described by extended Hückel Hamiltonians. The obtained steady-state currents were found to be in good agreement with predictions based on the Landauer formalism. The steady-state single-particle molecular state occupations have been analyzed in terms of their relative effective couplings to the left and right leads. For all cases studied, positivity of the reduced density matrix was conserved throughout the dynamics with no apparent violation of Pauli's exclusion principle. This indicates the robustness of the proposed approach for simulating electron dynamics in open quantum systems out of equilibrium. The extension of the DLvN approach presented herein is also important for future implementation of the method within density functional theory and density functional tight-binding computational codes, based on nonorthogonal basis-set

DOI: 10.1021/acs.jpcc.6b03838
J. Phys. Chem. C 2016, 120, 15052−15062

representations. This, in turn, will allow for accurate and efficient dynamic transport calculations in realistic molecular junction models.

APPENDIX A: CURRENT CALCULATION IN A NONORTHOGONAL BASIS-SET REPRESENTATION

The driven Liouville von Neumann equation in the state representation is given by

$$\frac{d}{dt}\begin{pmatrix} \tilde{\rho}_{L} & \tilde{\rho}_{L,EM} & \tilde{\rho}_{L,R} \\ \tilde{\rho}_{EM,L} & \tilde{\rho}_{EM} & \tilde{\rho}_{EM,R} \\ \tilde{\rho}_{R,L} & \tilde{\rho}_{R,EM} & \tilde{\rho}_{R} \end{pmatrix} = -\frac{i}{\hbar}\left[\begin{pmatrix} \tilde{\mathbf{H}}_{L} & \tilde{\mathbf{V}}_{L,EM} & \mathbf{0} \\ \tilde{\mathbf{V}}_{EM,L} & \tilde{\mathbf{H}}_{EM} & \tilde{\mathbf{V}}_{EM,R} \\ \mathbf{0} & \tilde{\mathbf{V}}_{R,EM} & \tilde{\mathbf{H}}_{R} \end{pmatrix}, \begin{pmatrix} \tilde{\rho}_{L} & \tilde{\rho}_{L,EM} & \tilde{\rho}_{L,R} \\ \tilde{\rho}_{EM,L} & \tilde{\rho}_{EM} & \tilde{\rho}_{EM,R} \\ \tilde{\rho}_{R,L} & \tilde{\rho}_{R,EM} & \tilde{\rho}_{R} \end{pmatrix}\right] - \Gamma\begin{pmatrix} \tilde{\rho}_{L} - \tilde{\rho}_{L}^{0} & \frac{1}{2}\tilde{\rho}_{L,EM} & \tilde{\rho}_{L,R} \\ \frac{1}{2}\tilde{\rho}_{EM,L} & \mathbf{0} & \frac{1}{2}\tilde{\rho}_{EM,R} \\ \tilde{\rho}_{R,L} & \frac{1}{2}\tilde{\rho}_{R,EM} & \tilde{\rho}_{R} - \tilde{\rho}_{R}^{0} \end{pmatrix} \tag{A1}$$

The dynamics of the density matrix block representing the extended molecule is thus given by

$$\frac{d\tilde{\boldsymbol{\rho}}_{EM}}{dt} = -\frac{i}{\hbar}[\tilde{\mathbf{H}}_{EM}, \tilde{\boldsymbol{\rho}}_{EM}] - \frac{i}{\hbar}(\tilde{\mathbf{V}}_{EM,L}\tilde{\boldsymbol{\rho}}_{L,EM} - \tilde{\boldsymbol{\rho}}_{EM,L}\tilde{\mathbf{V}}_{L,EM}) - \frac{i}{\hbar}(\tilde{\mathbf{V}}_{EM,R}\tilde{\boldsymbol{\rho}}_{R,EM} - \tilde{\boldsymbol{\rho}}_{EM,R}\tilde{\mathbf{V}}_{R,EM}) \tag{A2}$$

Since the MOs of the extended molecule are orthogonal to the lead section orbitals after the block orthogonalization procedure, the change in total number of electrons in the extended molecule region is given by

$$\dot{N}_{EM} = \frac{d}{dt}Tr(\tilde{\boldsymbol{\rho}}_{EM}) = Tr\left(\frac{d\tilde{\boldsymbol{\rho}}_{EM}}{dt}\right) = -\frac{i}{\hbar}Tr[\tilde{\mathbf{H}}_{EM}, \tilde{\boldsymbol{\rho}}_{EM}] - \frac{i}{\hbar}Tr(\tilde{\mathbf{V}}_{EM,L}\tilde{\boldsymbol{\rho}}_{L,EM} - \tilde{\boldsymbol{\rho}}_{EM,L}\tilde{\mathbf{V}}_{L,EM}) - \frac{i}{\hbar}Tr(\tilde{\mathbf{V}}_{EM,R}\tilde{\boldsymbol{\rho}}_{R,EM} - \tilde{\boldsymbol{\rho}}_{EM,R}\tilde{\mathbf{V}}_{R,EM}) \tag{A3}$$

Calculating each term separately we obtain

$$\begin{aligned} &Tr[\tilde{\mathbf{H}}_{EM}, \tilde{\boldsymbol{\rho}}_{EM}] \\ &= \sum_{n}^{N_{EM}}\left\{\sum_{m}^{N_{EM}}[\tilde{\mathbf{H}}_{EM}(n,m)\tilde{\boldsymbol{\rho}}_{EM}(m,n) - \tilde{\boldsymbol{\rho}}_{EM}(n,m)\tilde{\mathbf{H}}_{EM}(m,n)]\right\} \\ &= \sum_{n}^{N_{EM}}\sum_{m}^{N_{EM}}[\tilde{\mathbf{H}}_{EM}(n,m)\tilde{\boldsymbol{\rho}}_{EM}(m,n)] - \sum_{m}^{N_{EM}}\sum_{n}^{N_{EM}}[\tilde{\boldsymbol{\rho}}_{EM}(m,n)\tilde{\mathbf{H}}_{EM}(n,m)] \\ &= \sum_{n}^{N_{EM}}\sum_{m}^{N_{EM}}[\tilde{\mathbf{H}}_{EM}(n,m)\tilde{\boldsymbol{\rho}}_{EM}(m,n)] - \sum_{n}^{N_{EM}}\sum_{m}^{N_{EM}}[\tilde{\mathbf{H}}_{EM}(n,m)\tilde{\boldsymbol{\rho}}_{EM}(m,n)] = 0 \end{aligned} \tag{A4}$$

where summations run over the entire set of N_{EM} extended molecule states. Note that in the second equality we have switched between the summation indices of the second term. For the second term of eq A3 we have

$$\begin{aligned} &Tr(\tilde{\mathbf{V}}_{EM,L}\tilde{\boldsymbol{\rho}}_{L,EM} - \tilde{\boldsymbol{\rho}}_{EM,L}\tilde{\mathbf{V}}_{L,EM}) \\ &= \sum_{n}^{N_{EM}}\left\{\sum_{m}^{N_{L}}[\tilde{\mathbf{V}}_{EM,L}(n,m)\tilde{\boldsymbol{\rho}}_{L,EM}(m,n) - \tilde{\boldsymbol{\rho}}_{EM,L}(n,m)\tilde{\mathbf{V}}_{L,EM}(m,n)]\right\} \\ &= \sum_{n}^{N_{EM}}\sum_{m}^{N_{L}}[\tilde{\mathbf{V}}_{EM,L}(n,m)\tilde{\boldsymbol{\rho}}_{L,EM}(m,n) - \tilde{\boldsymbol{\rho}}_{L,EM}^{*}(m,n)\tilde{\mathbf{V}}_{EM,L}(n,m)] \\ &= \sum_{n}^{N_{EM}}\sum_{m}^{N_{L}}\tilde{\mathbf{V}}_{EM,L}(n,m)[\tilde{\boldsymbol{\rho}}_{L,EM}(m,n) - \tilde{\boldsymbol{\rho}}_{L,EM}^{*}(m,n)] \\ &= \sum_{n}^{N_{EM}}\sum_{m}^{N_{L}}\tilde{\mathbf{V}}_{EM,L}(n,m)2i\mathrm{Im}[\tilde{\boldsymbol{\rho}}_{L,EM}(m,n)] \\ &= 2i\sum_{n}^{N_{EM}}\sum_{m}^{N_{L}}\tilde{\mathbf{V}}_{EM,L}(n,m)\mathrm{Im}[\tilde{\boldsymbol{\rho}}_{L,EM}(m,n)] \end{aligned} \tag{A5}$$

Here, we have used the fact that the Hamiltonian matrix, in this case, is symmetric[91] ($\tilde{\mathbf{V}}_{L,EM}(m,n) = \tilde{\mathbf{V}}_{EM,L}(n,m)$) and the density matrix is Hermitian ($\tilde{\boldsymbol{\rho}}_{EM,L}(n,m) = \tilde{\boldsymbol{\rho}}_{L,EM}^{*}(m,n)$). Similarly, for the third term we obtain

$$\begin{aligned} &Tr(\tilde{\mathbf{V}}_{EM,R}\tilde{\boldsymbol{\rho}}_{R,EM} - \tilde{\boldsymbol{\rho}}_{EM,R}\tilde{\mathbf{V}}_{R,EM}) \\ &= 2i\sum_{n}^{N_{EM}}\sum_{m}^{N_{R}}\tilde{\mathbf{V}}_{EM,R}(n,m)\mathrm{Im}[\tilde{\boldsymbol{\rho}}_{R,EM}(m,n)] \\ &= -2i\sum_{n}^{N_{EM}}\sum_{m}^{N_{R}}\tilde{\mathbf{V}}_{R,EM}(m,n)\mathrm{Im}[\tilde{\boldsymbol{\rho}}_{EM,R}(n,m)] \end{aligned} \tag{A6}$$

Summing all terms and using the symmetry of the Hamiltonian matrix we have

$$\dot{N}_{EM} = \frac{d}{dt}Tr(\tilde{\boldsymbol{\rho}}_{EM}) = \frac{2}{\hbar}\sum_{n}^{N_{EM}}\sum_{m}^{N_{L}}\tilde{\mathbf{V}}_{L,EM}(m,n)\mathrm{Im}[\tilde{\boldsymbol{\rho}}_{L,EM}(m,n)] - \frac{2}{\hbar}\sum_{n}^{N_{EM}}\sum_{m}^{N_{R}}\tilde{\mathbf{V}}_{EM,R}(n,m)\mathrm{Im}[\tilde{\boldsymbol{\rho}}_{EM,R}(n,m)] \tag{A7}$$

We can now identify the term $(2/\hbar)\sum_{n}^{N_{EM}}\sum_{m}^{N_{L}}\tilde{\mathbf{V}}_{L,EM}(m,n)\mathrm{Im}[\tilde{\boldsymbol{\rho}}_{L,EM}(m,n)]$ as the net particle influx from the left lead into the extended molecule region and the term $(2/\hbar)\sum_{n}^{N_{EM}}\sum_{m}^{N_{R}}\tilde{\mathbf{V}}_{EM,R}(n,m)\mathrm{Im}[\tilde{\boldsymbol{\rho}}_{EM,R}(n,m)]$ as the net outgoing particle flux from the extended molecule region into the right lead. The total electric current can be defined as the average of these particle fluxes, multiplied by the charge, $|e|$, carried by each particle

$$\begin{aligned} J &= \frac{|e|}{2}\left\{\frac{2}{\hbar}\sum_{n}^{N_{EM}}\sum_{m}^{N_{L}}\tilde{\mathbf{V}}_{L,EM}(m,n)\mathrm{Im}[\tilde{\boldsymbol{\rho}}_{L,EM}(m,n)] + \frac{2}{\hbar}\sum_{n}^{N_{EM}}\sum_{m}^{N_{R}}\tilde{\mathbf{V}}_{EM,R}(n,m)\mathrm{Im}[\tilde{\boldsymbol{\rho}}_{EM,R}(n,m)]\right\} \\ &= \frac{|e|}{\hbar}\sum_{n}^{N_{EM}}\{-\sum_{m}^{N_{L}}\tilde{\mathbf{V}}_{EM,L}(n,m)\mathrm{Im}[\tilde{\boldsymbol{\rho}}_{EM,L}(n,m)] + \sum_{m}^{N_{R}}\tilde{\mathbf{V}}_{EM,R}(n,m)\mathrm{Im}[\tilde{\boldsymbol{\rho}}_{EM,R}(n,m)]\} \end{aligned} \tag{A8}$$

where we have used the symmetry of $\tilde{\mathbf{H}}$ and Hermiticity of $\tilde{\boldsymbol{\rho}}$ for the first term in the second line. If desired, this expression can be readily converted to the real-space (site) representation by the inverse of the basis transformations described in the main text to transform to the state-representation.

DOI: 10.1021/acs.jpcc.6b03838
J. Phys. Chem. C 2016, 120, 15052−15062

APPENDIX B: DESCRIPTION OF LANDAUER TRANSPORT CALCULATIONS IN NONORTHOGONAL BASIS-SET REPRESENTATIONS

The standard Landauer formalism was used to perform steady-state reference current calculations. In this approach, the current (I) flowing through the system from the left (L) lead to the right (R) lead at a given bias voltage (V) is evaluated from the probability, T, of an electron with a given energy, E, to traverse the system

$$I(V) = \frac{2e}{h}\int_{-\infty}^{\infty} dE[f_L(E, \mu_L(V)) - f_R(E, \mu_R(V))]T(E) \tag{B1}$$

where e is the electron charge; h is Planck's constant; $f_{L/R}(E, \mu_{L/R}(V)) = [1 + e^{\beta_{L/R}(E-\mu_{L/R}(V))}]$ are the Fermi–Dirac distribution functions representing the electron occupations in the left/right leads; $\beta_{L/R} = \frac{1}{k_B T_{L/R}}$; k_B is Boltzmann's constant; $T_{L/R}$ is the electronic temperature in the left/right leads; and the bias voltage is assumed to drop symmetrically at the lead–molecule junctions such that the lead chemical potentials $\mu_{L/R}$ are chosen as $\mu_{L/R} = E_f^{L/R} \pm 0.5$ V, with $E_f^{L/R}$ being the Fermi energy of the left/right lead.

The electron transmittance probability through the junctions, required as input for the Landauer formula, was calculated using the nonequilibrium Green's function trace formula[92−94]

$$T(E) = \mathrm{Tr}[\hat{\Gamma}_L(E)\hat{G}^r_{EM}(E)\hat{\Gamma}_R(E)\hat{G}^a_{EM}(E)] \tag{B2}$$

Here, $\hat{G}^r_{EM}(E) = [(\hat{G}^0_{EM}(E))^{-1} - \sum^r_L(E) - \sum^r_R(E)]^{-1}$ is the retarded Green's function of the extended molecule, where $\hat{G}^0_{EM}(E) = (E\hat{S}_{EM} - \hat{H}_{EM})^{-1}$ is the Green function of the bare extended molecule; $\hat{H}_{EM}$ is the Hamiltonian matrix representation of the extended molecule; $\hat{S}_{EM}$ is the overlap matrix representation of the extended molecule; and the lead self-energy functions $\sum^r_{L/R}(E)$ are given by

$$\hat{\Sigma}^r_{L/R}(E) = (E\hat{S}_{EM,L/R} - \hat{V}_{EM,L/R})\hat{G}^r_{L/R}(E)(E\hat{S}_{L/R,EM} - \hat{V}_{L/R,EM}) \tag{B3}$$

where $\hat{V}_{EM,L/R}$ is the Hamiltonian matrix block representing the coupling between the extended molecule and the left/right lead, $\hat{V}_{L/R,EM} = [\hat{V}_{EM,L/R}]^\dagger$; $\hat{S}_{EM,L/R}$ is the corresponding overlap matrix block; $\hat{S}_{L/R,EM} = [\hat{S}_{EM,L/R}]^\dagger$; and $\hat{G}^r_{L/R}(E) = (E\hat{S}_{L/R} - \hat{H}_{L/R})^{-1}$ is the retarded surface Green's function of the bare semi-infinite lead. The advanced Green's function matrix representation of the extended molecule is given by $\hat{G}^a_{EM}(E) = [\hat{G}^r_{EM}(E)]^\dagger$, and the broadening functions, $\hat{\Gamma}_{L/R}(E)$, are given by

$$\hat{\Gamma}_{L/R}(E) = i[\hat{\Sigma}^r_{L/R}(E) - \hat{\Sigma}^a_{L/R}(E)] \tag{B4}$$

with $\hat{\sum}^a_{L/R}(E) = [\hat{\sum}^r_{L/R}(E)]^\dagger$.

The retarded surface Green's function of the bare semi-infinite lead, $\hat{G}^r_{L/R}(E)$, can be obtained by using efficient iterative methods.[95−99] Here, in the spirit of the finite model system, we calculate it by complex matrix inversion of $\hat{G}^r_{L/R}(E) = [E\hat{S}_{L/R} - \hat{H}_{L/R} + i\eta_{L/R}]^{-1}$, where $\hat{H}_{L/R}$ is the Hamiltonian matrix representation of the finite left/right lead model; $\hat{S}_{L/R}$ is the overlap matrix representation of the finite left/right lead model; and $i\eta_{L/R}$ is a small imaginary broadening factor introduced to eliminate the singularities and broaden the discrete spectra of the finite lead models into a quasi-continuous one. To this end, $\eta_{L/R}$ is chosen as twice the maximum eigen-energy spacing within the Fermi transport region, defined by the chemical potentials and electronic temperatures of the lead model. The obtained Landauer current is then converged with respect to the size of the lead models to the required accuracy.

ASSOCIATED CONTENT

Supporting Information

The Supporting Information is available free of charge on the ACS Publications website at DOI: 10.1021/acs.jpcc.6b03838.

Transmittance probability of the gold/BDT/gold and gold/PDT/gold junctions plotted in a wide energy window; Isosurface plots of representative extended molecule MOs that span the junction region and can support current. Comparison of electron density variations obtained during the dynamics within the gold/BDT/gold and gold/PDT/gold junctions; Analysis of the correlation between the lead/extended-molecule state couplings and the extended molecule steady-state occupations (PDF)

Atomic coordinates of the gold/BDT/gold molecular junction model (XYZ)

Atomic coordinates of the gold/PDT/gold molecular junction model (XYZ)

AUTHOR INFORMATION

Corresponding Author

*E-mail: odedhod@tau.ac.il.

Present Address

§Department of Chemistry, New York University, New York, NY 10003, USA.

Notes

The authors declare no competing financial interest.

ACKNOWLEDGMENTS

We would like to thank Prof. Abraham Nitzan for many helpful discussions, Prof. Juan Carlos Cuevas for sharing with us the gold/BDT/gold junction coordinates, and Dr. Ariel Biller for help in the construction of the extended junction coordinates. Work at TAU was supported by the Israel Science Foundation under grant no. 1740/13, the Raymond and Beverly Sackler Fund for Convergence Research in Biomedical, Physical and Engineering Sciences, the Lise-Meitner Minerva Center for Computational Quantum Chemistry, and the Center for Nanoscience and Nanotechnology at Tel-Aviv University. Work at Weizmann was supported by the Israel Science Foundation and the Lise-Meitner Minerva Center for Computational Quantum Chemistry.

REFERENCES

(1) Aviram, A.; Ratner, M. A. Molecular Rectifiers. *Chem. Phys. Lett.* **1974**, *29*, 277−283.

(2) Nitzan, A. Electron Transmission Through Molecules and Molecular Interfaces. *Annu. Rev. Phys. Chem.* **2001**, *52*, 681−750.

(3) Ratner, M. A Brief History of Molecular Electronics. *Nat. Nanotechnol.* **2013**, *8*, 378−381.

(4) Bergfield, J. P.; Ratner, M. A. Forty Years of Molecular Electronics: Non-Equilibrium Heat and Charge Transport at the Nanoscale. *Phys. Status Solidi B* **2013**, *250*, 2249−2266.

DOI: 10.1021/acs.jpcc.6b03838
J. Phys. Chem. C 2016, 120, 15052−15062

(5) Cuevas, J. C.; Scheer, E. *Molecular Electronics: An Introduction to Theory and Experiment*; World Scientific, 2010.
(6) Aradhya, S. V.; Venkataraman, L. Single-Molecule Junctions Beyond Electronic Transport. *Nat. Nanotechnol.* **2013**, *8*, 399−410.
(7) Sun, L.; Diaz-Fernandez, Y. A.; Gschneidtner, T. A.; Westerlund, F.; Lara-Avila, S.; Moth-Poulsen, K. Single-Molecule Electronics: from Chemical Design to Functional Devices. *Chem. Soc. Rev.* **2014**, *43*, 7378−7411.
(8) Quek, S. Y.; Kamenetska, M.; Steigerwald, M. L.; Choi, H. J.; Louie, S. G.; Hybertsen, M. S.; Neaton, J. B.; Venkataraman, L. Mechanically Controlled Binary Conductance Switching of a Single-Molecule Junction. *Nat. Nanotechnol.* **2009**, *4*, 230−234.
(9) Fuentes, N.; Martin-Lasanta, A.; de Cienfuegos, L. A.; Ribagorda, M.; Parra, A.; Cuerva, J. M. Organic-Based Molecular Switches for Molecular Electronics. *Nanoscale* **2011**, *3*, 4003−4014.
(10) Petrov, E. G.; Leonov, V. O.; Snitsarev, V. Transient Photocurrent in Molecular Junctions: Singlet Switching On and Triplet Blocking. *J. Chem. Phys.* **2013**, *138*, 184709.
(11) Sotthewes, K.; Geskin, V.; Heimbuch, R.; Kumar, A.; Zandvliet, H. J. W. Research Update: Molecular Electronics: The Single-Molecule Switch and Transistor. *APL Mater.* **2014**, *2*, 010701.
(12) Li, Z. H.; Li, H.; Chen, S. J.; Froehlich, T.; Yi, C. Y.; Schonenberger, C.; Calame, M.; Decurtins, S.; Liu, S. X.; Borguet, E. Regulating a Benzodifuran Single Molecule Redox Switch via Electrochemical Gating and Optimization of Molecule/Electrode Coupling. *J. Am. Chem. Soc.* **2014**, *136*, 8867−8870.
(13) Lehmann, J.; Kohler, S.; Hänggi, P.; Nitzan, A. Molecular Wires Acting as Coherent Quantum Ratchets. *Phys. Rev. Lett.* **2002**, *88*, 228305.
(14) Lehmann, J.; Kohler, S.; Hanggi, P.; Nitzan, A. Rectification of Laser-Induced Electronic Transport Through Molecules. *J. Chem. Phys.* **2003**, *118*, 3283−3293.
(15) Batra, A.; Darancet, P.; Chen, Q. S.; Meisner, J. S.; Widawsky, J. R.; Neaton, J. B.; Nuckolls, C.; Venkataraman, L. Tuning Rectification in Single-Molecular Diodes. *Nano Lett.* **2013**, *13*, 6233−6237.
(16) Capozzi, B.; Xia, J. L.; Adak, O.; Dell, E. J.; Liu, Z. F.; Taylor, J. C.; Neaton, J. B.; Campos, L. M.; Venkataraman, L. Single-Molecule Diodes With High Rectification Ratios Through Environmental Control. *Nat. Nanotechnol.* **2015**, *10*, 522−527.
(17) Zhang, G. B.; Ratner, M. A.; Reuter, M. G. Is Molecular Rectification Caused by Asymmetric Electrode Couplings or by a Molecular Bias Drop? *J. Phys. Chem. C* **2015**, *119*, 6254−6260.
(18) Yuan, L.; Nerngchamnong, N.; Cao, L.; Hamoudi, H.; del Barco, E.; Roemer, M.; Sriramula, R. K.; Thompson, D.; Nijhuis, C. A. Controlling the Direction of Rectification in a Molecular Diode. *Nat. Commun.* **2015**, *6*, 6324.
(19) Dubi, Y.; Di Ventra, M. Thermoelectric Effects in Nanoscale Junctions. *Nano Lett.* **2009**, *9*, 97−101.
(20) Entin-Wohlman, O.; Imry, Y.; Aharony, A. Three-Terminal Thermoelectric Transport through a Molecular Junction. *Phys. Rev. B: Condens. Matter Mater. Phys.* **2010**, *82*, 115314.
(21) Widawsky, J. R.; Darancet, P.; Neaton, J. B.; Venkataraman, L. Simultaneous Determination of Conductance and Thermopower of Single Molecule Junctions. *Nano Lett.* **2012**, *12*, 354−358.
(22) Lee, W.; Kim, K.; Jeong, W.; Zotti, L. A.; Pauly, F.; Cuevas, J. C.; Reddy, P. Heat Dissipation in Atomic-Scale Junctions. *Nature* **2013**, *498*, 209−212.
(23) Dubi, Y. Possible Origin of Thermoelectric Response Fluctuations in Single-Molecule Junctions. *New J. Phys.* **2013**, *15*, 105004.
(24) Vacek, J.; Chocholousova, J. V.; Stara, I. G.; Stary, I.; Dubi, Y. Mechanical Tuning of Conductance and Thermopower in Helicene Molecular Junctions. *Nanoscale* **2015**, *7*, 8793−8802.
(25) Solomon, G. C.; Herrmann, C.; Hansen, T.; Mujica, V.; Ratner, M. A. Exploring Local Currents in Molecular Junctions. *Nat. Chem.* **2010**, *2*, 223−228.
(26) Xia, J. L.; Capozzi, B.; Wei, S. J.; Strange, M.; Batra, A.; Moreno, J. R.; Amir, R. J.; Amir, E.; Solomon, G. C.; Venkataraman, L.; Campos, L. M. Breakdown of Interference Rules in Azulene, a Nonalternant Hydrocarbon. *Nano Lett.* **2014**, *14*, 2941−2945.
(27) Reuter, M. G.; Hansen, T. Communication: Finding Destructive Interference Features in Molecular Transport Junctions. *J. Chem. Phys.* **2014**, *141*, 181103.
(28) Pedersen, K. G. L.; Borges, A.; Hedegard, P.; Solomon, G. C.; Strange, M. Illusory Connection Between Cross-Conjugation and Quantum Interference. *J. Phys. Chem. C* **2015**, *119*, 26919−26924.
(29) Su, T. A.; Neupane, M.; Steigerwald, M. L.; Venkataraman, L.; Nuckolls, C. Chemical Principles of Single-Molecule Electronics. *Nat. Rev. Mater.* **2016**, *1*, 16002.
(30) Cahen, D.; Kahn, A. Electron Energetics at Surfaces and Interfaces: Concepts and Experiments. *Adv. Mater.* **2003**, *15*, 271−277.
(31) Kronik, L.; Koch, N. Electronic Properties of Organic-Based Interfaces. *MRS Bull.* **2010**, *35*, 417−419.
(32) Jia, C. C.; Guo, X. F. Molecule-Electrode Interfaces in Molecular Electronic Devices. *Chem. Soc. Rev.* **2013**, *42*, 5642−5660.
(33) Yelin, T.; Korytár, R.; Sukenik, N.; Vardimon, R.; Kumar, B.; Nuckolls, C.; Evers, F.; Tal, O. Conductance Saturation in a Series of Highly Transmitting Molecular Junctions. *Nat. Mater.* **2016**, *15*, 444−449.
(34) Galperin, M.; Nitzan, A. Current-Induced Light Emission and Light-induced Current in Molecular-Tunneling Junctions. *Phys. Rev. Lett.* **2005**, *95*, 206802.
(35) Kleinekathofer, U.; Li, G.; Welack, S.; Schreiber, M. Switching the Current Through Model Molecular Wires with Gaussian Laser Pulses. *Europhys. Lett.* **2006**, *75*, 139−145.
(36) Kleinekathöfer, U.; Li, G. Q.; Welack, S.; Schreiber, M. Coherent Destruction of the Current Through Molecular Wires Using Short Laser Pulses. *Phys. Status Solidi B* **2006**, *243*, 3775−3781.
(37) Fainberg, B. D.; Jouravlev, M.; Nitzan, A. Light-Induced Current in Molecular Tunneling Junctions Excited with Intense Shaped Pulses. *Phys. Rev. B: Condens. Matter Mater. Phys.* **2007**, *76*, 245329.
(38) Subotnik, J. E.; Hansen, T.; Ratner, M. A.; Nitzan, A. Nonequilibrium Steady State Transport via the Reduced Density Matrix Operator. *J. Chem. Phys.* **2009**, *130*, 144105.
(39) Rothman, A. E.; Mazziotti, D. A. Nonequilibrium, Steady-State Electron Transport With N-Representable Density Matrices From the Anti-Hermitian Contracted Schroumldinger Equation. *J. Chem. Phys.* **2010**, *132*, 104112.
(40) Volkovich, R.; Peskin, U. Transient Dynamics in Molecular Junctions: Coherent Bichromophoric Molecular Electron Pumps. *Phys. Rev. B: Condens. Matter Mater. Phys.* **2011**, *83*, 033403.
(41) Renaud, N.; Ratner, M. A.; Joachim, C. A Time-Dependent Approach to Electronic Transmission in Model Molecular Junctions. *J. Phys. Chem. B* **2011**, *115*, 5582−5592.
(42) Peskin, U.; Galperin, M. Coherently Controlled Molecular Junctions. *J. Chem. Phys.* **2012**, *136*, 044107.
(43) Nguyen, T. S.; Nanguneri, R.; Parkhill, J. How Electronic Dynamics With Pauli Exclusion Produces Fermi−Dirac Statistics. *J. Chem. Phys.* **2015**, *142*, 134113.
(44) Baer, R.; Neuhauser, D. Ab Initio Electrical Conductance of a Molecular Wire. *Int. J. Quantum Chem.* **2003**, *91*, 524−532.
(45) Baer, R.; Seideman, T.; Ilani, S.; Neuhauser, D. Ab initio Study of the Alternating Current Impedance of a Molecular Junction. *J. Chem. Phys.* **2004**, *120*, 3387−3396.
(46) Di Ventra, M.; Todorov, T. N. Transport in Nanoscale Systems: the Microcanonical versus Grand-Canonical Picture. *J. Phys.: Condens. Matter* **2004**, *16*, 8025−8034.
(47) Bushong, N.; Sai, N.; Di Ventra, M. Approach to Steady-State Transport in Nanoscale Conductors. *Nano Lett.* **2005**, *5*, 2569−2572.
(48) Sánchez, C. G.; Stamenova, M.; Sanvito, S.; Bowler, D. R.; Horsfield, A. P.; Todorov, T. N. Molecular Conduction: Do Time-Dependent Simulations Tell You More Than the Landauer Approach? *J. Chem. Phys.* **2006**, *124*, 214708.

DOI: 10.1021/acs.jpcc.6b03838
J. Phys. Chem. C 2016, 120, 15052−15062

(49) Zheng, X.; Wang, F.; Yam, C. Y.; Mo, Y.; Chen, G. H. Time-Dependent Density-Functional Theory for Open Systems. *Phys. Rev. B: Condens. Matter Mater. Phys.* **2007**, *75*, 195127.
(50) Evans, J. S.; Van Voorhis, T. Dynamic Current Suppression and Gate Voltage Response in Metal-Molecule-Metal Junctions. *Nano Lett.* **2009**, *9*, 2671−2675.
(51) Ercan, I.; Anderson, N. G. Tight-Binding Implementation of the Microcanonical Approach to Transport in Nanoscale Conductors: Generalization and Analysis. *J. Appl. Phys.* **2010**, *107*, 124318.
(52) Zheng, X. A.; Chen, G. H.; Mo, Y.; Koo, S. K.; Tian, H.; Yam, C.; Yan, Y. J. Time-Dependent Density Functional Theory for Quantum Transport. *J. Chem. Phys.* **2010**, *133*, 114101.
(53) Ke, S. H.; Liu, R.; Yang, W. T.; Baranger, H. U. Time-Dependent Transport Through Molecular Junctions. *J. Chem. Phys.* **2010**, *132*, 234105.
(54) Xing, Y.; Wang, B.; Wang, J. First-Principles Investigation of Dynamical Properties of Molecular Devices Under a Steplike Pulse. *Phys. Rev. B: Condens. Matter Mater. Phys.* **2010**, *82*, 205112.
(55) Wang, R. L.; Hou, D.; Zheng, X. Time-Dependent Density-Functional Theory For Real-Time Electronic Dynamics on Material Surfaces. *Phys. Rev. B: Condens. Matter Mater. Phys.* **2013**, *88*, 205126.
(56) Schaffhauser, P.; Kümmel, S. Using Time-Dependent Density Functional Theory in Real Time for Calculating Electronic Transport. *Phys. Rev. B: Condens. Matter Mater. Phys.* **2016**, *93*, 035115.
(57) Zelovich, T.; Kronik, L.; Hod, O. State Representation Approach for Atomistic Time-Dependent Transport Calculations in Molecular Junctions. *J. Chem. Theory Comput.* **2014**, *10*, 2927−2941.
(58) Zelovich, T.; Kronik, L.; Hod, O. Molecule-Lead Coupling at Molecular Junctions: Relation Between the Real- and State-Space Perspectives. *J. Chem. Theory Comput.* **2015**, *11*, 4861−4869.
(59) Chen, L. P.; Hansen, T.; Franco, I. Simple and Accurate Method for Time-Dependent Transport along Nanoscale Junctions. *J. Phys. Chem. C* **2014**, *118*, 20009−20017.
(60) Varga, K. Time-Dependent Density Functional Study of Transport in Molecular Junctions. *Phys. Rev. B: Condens. Matter Mater. Phys.* **2011**, *83*, 195130.
(61) Wang, Y.; Yam, C. Y.; Frauenheim, T.; Chen, G. H.; Niehaus, T. A. An Efficient Method for Quantum Transport Simulations in the Time Domain. *Chem. Phys.* **2011**, *391*, 69−77.
(62) Kwok, Y. H.; Xie, H.; Yam, C. Y.; Zheng, X.; Chen, G. H. Time-Dependent Density Functional Theory Quantum Transport Simulation in Non-Orthogonal Basis. *J. Chem. Phys.* **2013**, *139*, 224111.
(63) Cao, H.; Zhang, M. D.; Tao, T.; Song, M. X.; Zhang, C. Z. Electric Response of a Metal-Molecule-Metal Junction to Laser Pulse by Solving Hierarchical Equations of Motion. *J. Chem. Phys.* **2015**, *142*, 084705.
(64) Peralta, J. E.; Hod, O.; Scuseria, G. E. Magnetization Dynamics from Time-Dependent Noncollinear Spin Density Functional Theory Calculations. *J. Chem. Theory Comput.* **2015**, *11*, 3661−3668.
(65) Oviedo, M. B.; Wong, B. M. Real-Time Quantum Dynamics Reveals Complex, Many-Body Interactions in Solvated Nanodroplets. *J. Chem. Theory Comput.* **2016**, *12*, 1862−1871.
(66) Hod, O.; Rodríguez-Rosario, C. A.; Zelovich, T.; Frauenheim, T. Driven Liouville Von Neumann Equation in Lindblad Form. *J. Phys. Chem. A* **2016**, *120*, 3278−3285.
(67) Hoffmann, R. An Extended Huckel Theory. I. Hydrocarbons. *J. Chem. Phys.* **1963**, *39*, 1397−1412.
(68) Whangbo, M. H. Perspective on "An Extended Huckel Theory. I. Hydrocarbons" - Hoffmann R. *J. Chem. Phys.* **1963**, *39*, 1397−1412; *Theor. Chem. Acc.* **2000**, *103*, 252−256.
(69) Cerda, J.; Soria, F. Accurate and Transferable Extended Huckel Type Tight-Binding Parameters. *Phys. Rev. B: Condens. Matter Mater. Phys.* **2000**, *61*, 7965−7971.
(70) Martins, A. D.; Verissimo-Alves, M. Group-IV Nanosheets With Vacancies: A Tight-Binding Extended Huckel Study. *J. Phys.: Condens. Matter* **2014**, *26*, 365501.
(71) Ribeiro, I. A.; Ribeiro, F. J.; Martins, A. S. An Extended Huckel Study of the Electronic Properties of III-V Compounds and Their Alloys. *Solid State Commun.* **2014**, *186*, 50−55.
(72) Viljas, J. K.; Cuevas, J. C.; Pauly, F.; Hafner, M. Electron-vibration interaction in transport through atomic gold wires. *Phys. Rev. B: Condens. Matter Mater. Phys.* **2005**, *72*, 245415.
(73) London, F. Quantum Theory of Interatomic Currents in Aromatic Compounds. *J. Phys. Radium* **1937**, *8*, 397.
(74) Pople, J. A. Molecular Orbital Theory of Diamagnetism: I. An Approximate LCAO Scheme. *J. Chem. Phys.* **1962**, *37*, 53−59.
(75) Wolfsberg, M.; Helmholz, L. The Spectra and Electronic Structure of the Tetrahedral Ions MnO_4^-, CrO_4^-, and ClO_4^-. *J. Chem. Phys.* **1952**, *20*, 837−843.
(76) Guseinov, I. I. Analytical Evaluation of 2-Centre Coulomb, Hybrid and One-Electron Integrals for Slater-Type Orbitals. *J. Phys. B: At. Mol. Phys.* **1970**, *3*, 1399−1412.
(77) Guseinov, I. I. Evaluation of 2-Center Overlap and Nuclear-Attraction Integrals for Slater-Type Orbitals. *Phys. Rev. A: At., Mol., Opt. Phys.* **1985**, *32*, 1864−1866.
(78) Guseinov, I. I. Analytical Evaluation of Molecular Electric and Magnetic Multipole Moment Integrals Over Slater-Type Orbitals. *Int. J. Quantum Chem.* **1998**, *68*, 145−150.
(79) Guseinov, I. I.; Mamedov, B. A. Computation of Molecular Integrals Over Slater Type Orbitals - I. Calculations of Overlap Integrals Using Recurrence Relations. *J. Mol. Struct.: THEOCHEM* **1999**, *465*, 1−6.
(80) Guseinov, I. I. Response to the Comment: On the Computation of Molecular Auxiliary Functions A_n and B_n. *Pramana* **2003**, *61*, C781−C783.
(81) Hod, O. Molecular Nano-electronic Devices Based on Aharonov-Bohm Interferometry, Ph.D. Thesis. Tel-Aviv University, 2005.
(82) http://www.quantumwise.com/documents/manuals/ATK-2014/ReferenceManual/index.html/chap.atomicdata.html#sect3.atomicdata.huckel.hoffmann; Hoffmann Hückel basis-set parameters.
(83) As discussed in ref 38 the proper choice of lead model size is dictated by the lead/molecule coupling. In practice, one should converge the property of interest, e.g., current or state occupations, with respect to the finite lead model size.
(84) Li, G. Q.; Schreiber, M.; Kleinekathöfer, U. Coherent Laser Control of the Current Through Molecular Junctions. *Europhys. Lett.* **2007**, *79*, 27006.
(85) Landauer, R. Spatial Variation of Currents and Fields Due to Localized Scatterers in Metallic Conduction. *IBM J. Res. Dev.* **1957**, *1*, 223−231.
(86) Büttiker, M. Four-Terminal Phase-Coherent Conductance. *Phys. Rev. Lett.* **1986**, *57*, 1761−1764.
(87) The agreement between the steady-state lead occupations and the target population function can be further improved by increasing the lead model size.
(88) Zotti, L. A.; Burkle, M.; Pauly, F.; Lee, W.; Kim, K.; Jeong, W.; Asai, Y.; Reddy, P.; Cuevas, J. C. Heat Dissipation and its Relation to Thermopower in Single-Molecule Junctions. *New J. Phys.* **2014**, *16*, 015004.
(89) Liu, R.; Wang, C.-K.; Li, Z.-L. A Method to Study Electronic Transport Properties of Molecular Junction: One-Dimension Transmission Combined with Three-Dimension Correction Approximation (OTCTCA). *Sci. Rep.* **2016**, *6*, 21946.
(90) In practice, the effect of the deviations from the lead target occupations in the two leads tends to balance with small effect on the calculated currents within the extended molecule region. Hence one should converge the measured property with respect to the finite lead model size.
(91) When considering magnetic fields, complex gauge invariant atomic orbitals are often used, and the Hamiltonian matrix becomes complex Hermitian

DOI: 10.1021/acs.jpcc.6b03838
J. Phys. Chem. C 2016, 120, 15052−15062

(92) Datta, S. *Electronic Transport in Mesoscopic Systems*; Cambridge University Press: Cambridge, 1995.
(93) Paulsson, M. Non Equilibrium Green's Functions for Dummies: Introduction to the One Particle NEGF Equations. arXiv:cond-mat/0210519v2, 2006.
(94) D'Agosta, R.; Di Ventra, M. Stochastic Time-Dependent Current-Density-Functional Theory: A Functional Theory of Open Qquantum Systems. *Phys. Rev. B: Condens. Matter Mater. Phys.* **2008**, *78*, 165105.
(95) Lee, D. H.; Joannopoulos, J. D. Simple Scheme for Surface-Band Calculations II. The Greens-Function. *Phys. Rev. B: Condens. Matter Mater. Phys.* **1981**, *23*, 4997−5004.
(96) Sancho, M. P. L.; Sancho, J. M. L.; Rubio, J. Quick Iterative Scheme for the Calculation of Transfer-Matrices - Application to Mo(100). *J. Phys. F: Met. Phys.* **1984**, *14*, 1205−1215.
(97) Sancho, M. P. L.; Sancho, J. M. L.; Rubio, J. Highly Convergent Schemes for the Calculation of Bulk and Surface Green-Functions. *J. Phys. F: Met. Phys.* **1985**, *15*, 851−858.
(98) Nardelli, M. B. Electronic Transport in Extended Systems: Application to Carbon Nanotubes. *Phys. Rev. B: Condens. Matter Mater. Phys.* **1999**, *60*, 7828−7833.
(99) Cheng, C. L.; Evans, J. S.; Van Voorhis, T. Simulating Molecular Conductance Using Real-Time Density Functional Theory. *Phys. Rev. B: Condens. Matter Mater. Phys.* **2006**, *74*, 155112.

DOI: 10.1021/acs.jpcc.6b03838
J. Phys. Chem. C 2016, 120, 15052−15062